3D-Mapping and Manipulation of Photocurrent in an Optoelectronic Diamond Device

Alexander A. Wood,* Daniel J. McCloskey, Nikolai Dontschuk, Artur Lozovoi, Russell M. Goldblatt, Tom Delord, David A. Broadway, Jean-Philippe Tetienne, Brett C. Johnson, Kaih T. Mitchell, Christopher T.-K. Lew, Carlos A. Meriles, and Andy M. Martin

Establishing connections between material impurities and charge transport properties in emerging electronic and quantum materials, such as wide-bandgap semiconductors, demands new diagnostic methods tailored to these unique systems. Many such materials host optically-active defect centers which offer a powerful in situ characterization system, but one that typically relies on the weak spin-electric field coupling to measure electronic phenomena. In this work, charge-state sensitive optical microscopy is combined with photoelectric detection of an array of nitrogen-vacancy (NV) centers to directly image the flow of charge carriers inside a diamond optoelectronic device, in 3D and with temporal resolution. Optical control is used to change the charge state of background impurities inside the diamond on-demand, resulting in drastically different current flow such as filamentary channels nucleating from specific, defective regions of the device. Conducting channels that control carrier flow, key steps toward optically reconfigurable, wide-bandgap optoelectronics are then engineered using light. This work might be extended to probe other wide-bandgap semiconductors (SiC, GaN) relevant to present and emerging electronic and quantum technologies.

A. A. Wood, D. J. McCloskey, N. Dontschuk, R. M. Goldblatt,
K. T. Mitchell, C. T.-K. Lew, A. M. Martin
School of Physics
University of Melbourne
Parkville, Victoria 3010, Australia
E-mail: alexander.wood@unimelb.edu.au
A. Lozovoi, T. Delord, C. A. Meriles
CUNY-The City College of New York
New York 10031, USA
D. A. Broadway, J.-P. Tetienne, B. C. Johnson
School of Science
RMIT University
Melbourne, Victoria 3000, Australia
C. A. Meriles
CUNY - The Graduate Center
New York, NY 10016, USA

1. Introduction

Characterizing a material, however exotic, for use in electronics applications amounts to determining how charges enter, leave, and – most importantly – move through it. An ideal diagnostic platform would thus consist of an array of in-built, minimally-perturbative detectors embedded throughout a material that detect charges as they traverse the device. Exactly this situation occurs in several wide-bandgap semiconductors, where impurities give rise to optically-active defect centers[1–3] distributed throughout the material. Some of these defects even exhibit coherent spin properties at room temperature,[4] such as the NV center in diamond[5] or the silicon-vacancy and divacancy in SiC.[6,7] Recently, it has been shown that exploiting the spin properties of these defects provides a powerful means of characterizing electronic properties of both the host material[8–11] and semiconductor devices external to the host via the magnetic signatures of currents.[12–16]

However, optically-based spin measurements of charge transport are too insensitive and perturbative to employ for the electrical detection of transient, dynamical conduction processes such as electrical breakdown *inside* the host material. In the case of wide-bandgap materials such as diamond, SiC, and GaN that have emerging applications in high-power electronics,[17–19] new in situ probes could help unravel material interface properties and charge carrier dynamics central to electrical performance. Compared to the spin, the electronic charge state of a deep-level defect in a wide-bandgap semiconductor is a stable and optically addressable resource[20,21] for the study of charge transport.[22,23] Besides their impact on transport properties, the charge of semiconductor defects plays a critical role in quantum sensing and quantum information,[24] with significant effort put into controlling,[25,26] stabilizing[27,28] and understanding[29,30] their charge state and charge environment. In this work, we use single-shot, non-perturbative charge-sensitive optical microscopy to reveal the generation and flow of electric currents inside a wide-bandgap semiconductor at room temperature and in three dimensions. Our technique is distinct from scanning

**ADVANCED
SCIENCE NEWS**

www.advancedsciencenews.com
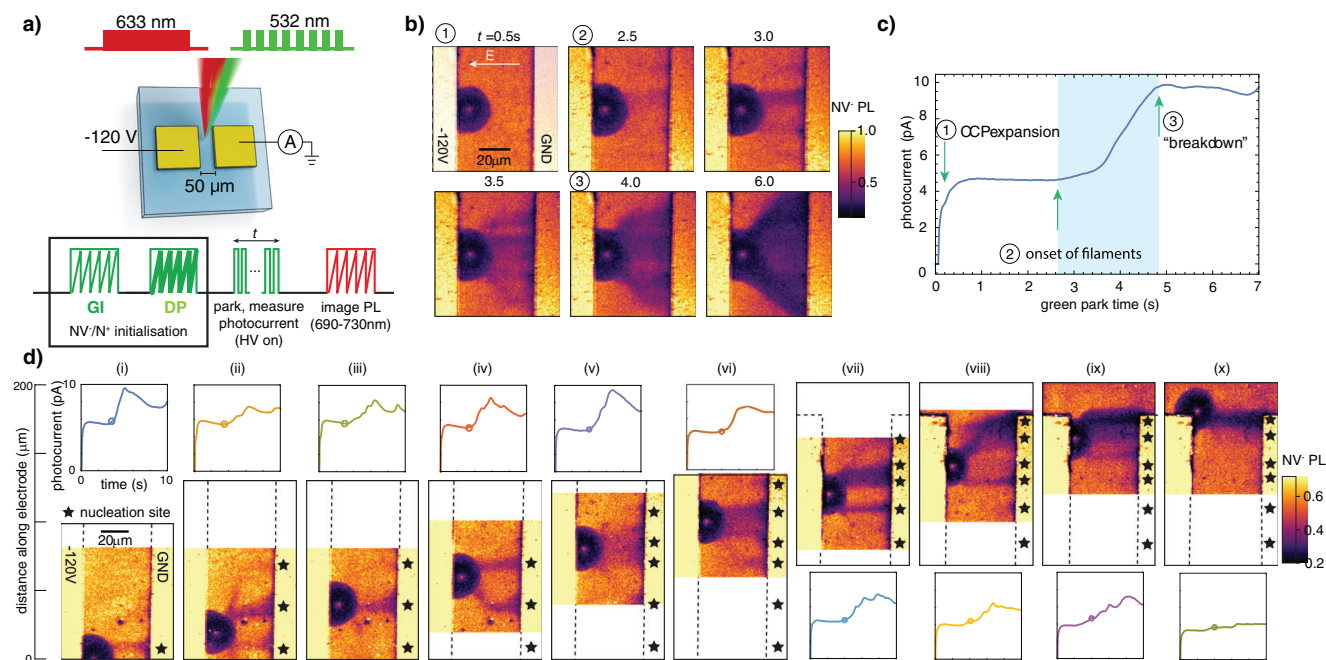
**ADVANCED
MATERIALS**

www.advmat.de

Figure 1. Photocurrent generation and detection within an optoelectronic diamond device. a) Experimental setup: two planar electrodes are deposited on the surface of a diamond hosting NV centers. Optical protocols (bottom frame) are used to prepare the NV centers and other defects in particular charge states, which can then be measured using optical confocal microscopy or detection of photocurrent via the electrodes and lock-in amplification. HV on denotes high voltage applied to the electrode. b) Images of NV⁻ photoluminescence after an 8 mW (80 Hz modulated) green laser beam is positioned near the left electrode, held at −120 V, while the right-hand electrode (positive) connects to ground through a current amplifier, and c) corresponding photocurrent versus time. All images are 80 × 80 μm scans. The formation of dark, NV⁰-rich filaments connecting the charge capture halo surrounding the illumination spot to the left-hand electrode is correlated with distinct features in the photocurrent, which corresponds to predominantly-hole photocurrent flowing in local channels before a general "breakdown" event at later times. Holes move from right to left in these images. The semicircular shape of the nominally symmetric CCP is a result of the left-hand electrode obscuring the imaging region. d) (i–x) The dark filaments nucleate from specific regions of the electrodes, as these scans over a 200 μm region show. Plots of the time-dependent photocurrent are shown inset for each confocal scan, and the colored circle on each plot indicates the corresponding time where the image is taken (3–4.5 s, where the filaments are most clearly resolved for each case). At each point, the onset of filaments always precedes a general increase in photocurrent.

photocurrent microscopy, where optical excitation generates a photocurrent signal at remote electrodes:[31] here, we image the actual photocurrent as it flows between electrical contacts and the point of optical illumination, a measurement simultaneously in situ yet also weakly perturbing.

Our method works on the basis that a charge carrier induces a measurable change in the fluorescence of a color center defect upon capture, for instance NV⁻ + h⁺ → NV⁰. With charge-state selective excitation and spectral filtering, we detect only the NV⁻ fluorescence, consequently, the spatial profile and time evolution of current flow is imprinted on the charge state of an ensemble of NV centers embedded throughout the device, enabling microscale mapping in three dimensions. Optical confocal microscopy is augmented by the simultaneous electrical detection of time-dependent currents, allowing us to make clear associations between spatial structures observed in images and current transients. We employ our technique to detect local electric field inhomogeneities and preferential charge injection in a metal-semiconductor interface, revealing points in the metal-diamond junction that unexpectedly nucleate thin filament-like channels of charge carriers. Next, we show that the spatial structure and temporal variation of photocurrent is determined by the charge state of nonfluorescent nitrogen impurities,[32] which can be optically prepared into space-charge regions that impede current

flow or a charge-neutral, high-mobility background. We can control and even mimic the naturally-occurring filament structures by creating optically-defined patterns of varied conductivity with laser scans, and then image the effects on charge transport created by these patterns in three spatial dimensions with temporal resolution.

2. Results

Our experiment, depicted schematically in **Figure 1a** and detailed further in Experimental Methods, uses a diamond sample equipped with a pair of coplanar Au/Cr electrodes (500 × 500 μm, 50 μm spacing) fabricated on the oxygen-terminated diamond surface via photolithography (see Experimental Methods). The nitrogen and NV concentrations are 1 and 0.01 ppm, respectively. A purpose-built confocal microscope enables two-color optical illumination (532 and 633 nm) and charge-state-selective imaging via collection of only NV⁻ fluorescence within a limited band (691–731 nm). One of the electrodes is held at a potential V, while the other connects to the ground via a low-noise current preamplifier and lock-in amplifier in a standard setup to detect photocurrent.[33,34] The voltage–current characteristics of the device were found to exhibit the characteristic back-to-back Schottky-diode shape of similar semiconductor-metal

interface devices,[35] preventing efficient injection of charge into the diamond from the electrodes. We thus generated a photocurrent inside the diamond using optical illumination and charge cycling[36] of the NV centers, which injects free electrons and holes into the conduction and valence bands of the diamond, respectively. These freely-diffusing charge carriers are then trapped by various defects, or drift toward the electrodes and are detected as a photocurrent.[37] In the former case, and in the absence of an electric field, positively-charged holes are efficiently captured by negatively-charged NV^- centers, resulting in a characteristic "halo"-like f (CCP) of NV^0 and thus reduced fluorescence around the illumination point in an NV^--selective image. Combining photoelectric detection with charge-sensitive imaging allows us to then track where photocurrent flows when an electric field is applied.

Prior to inducing the photocurrent, we use a two-step initialization process to prepare the NV and nitrogen in the sample into consistent charge states, as depicted in Figure 1a. The first step, green initialization (GI) converts NV^- into NV^0[20,21,38] and N^+ into N^0,[39,40] effectively erasing any prior charge patterns. The second step, defocus preparation (DP) converts from NV^0 into NV^-[38,41] and N^0 into N^+,[42] leaving an NV^-/N^+ charge environment upon which all experiments are conducted. While the charge state of the NV center can be readily identified optically, we infer the charge state of nitrogen created by the initialization protocols based on the presence of free carriers generated by the scanning laser, as discussed below. Though other defects are expected to play a similar role,[42] we focus on nitrogen given it is the highest abundance impurity in our sample. A full understanding of the charge environment we initialize necessarily includes consideration of other defects, including vacancies, as discussed later.

Briefly, in GI an 8 mW green laser beam is scanned a few micrometers below the diamond surface over an $(80 \mu m)^2$ region. As the laser scans, it drives rapid NV charge cycling that generates electrons and holes which diffuse away almost symmetrically in three dimensions. In the wake of the scanning laser, NV^0 is generated via hole capture by NV^-,[38] while we anticipate N^0 generation via electron capture by N^+.[39,40] GI serves to delete any prior charge patterns mapped onto the diamond. Subsequently, for DP initialization, the microscope objective is elevated 50 μm above the scanning plane and the process is repeated. This time, however, the significantly lower intensity (10^4–10^5 W cm^{-2}) suppresses NV charge cycling (as a two-photon process for green light it is proportional to I^2)[36] and thus only single-photon ionization of nitrogen occurs, $N^0 \rightarrow N^+ + e^-$. The liberated electron is prevented from being recaptured by N^+ due to the sustained green illumination over the wide area of the defocused laser beam and is eventually trapped by NV^0 to form NV^-. Thus, the DP step initializes a charge environment dominated by NV^- and N^+. Typical scans take 30 s to complete, and the electric field is off during the initialization scans. Further details can be found in the Supporting Information.

After initialization, we apply a –120 V bias voltage to the left-hand electrode and position a focused green laser beam (8 mW, 1 μm diameter) near the same electrode for a variable duration. The position of the laser beam was chosen to maximize the measured steady-state photocurrent (see Supporting Information). The green light is modulated at 80 Hz to facilitate lock-in detection of the photocurrent, the modulation itself was not observed to have any confounding effects on the measurements. While the measured photocurrent is suggested to originate from various sources,[43] we verified that NV charge cycling in fact contributes a significant fraction by performing a photoelectrically-detected magnetic resonance (PDMR) measurement with an applied microwave field and measuring the optical power dependence of the photocurrent (see Supporting Information). The presence of a PDMR signal and an almost entirely quadratic dependence on green optical power, characteristic of two-photon mediated NV charge cycling under green light,[34,36] confirms that NV charge cycling injects a significant fraction of the photocurrent we measure in our experiments.

The charge carrier dynamics terminate immediately upon extinguishing the laser, and the photocurrent spatial dynamics up to a given time are thus frozen in the charge distribution of the NV centers. We then perform charge-sensitive imaging by scanning a weak red laser (50 μW, 633 nm) over the same ($80 \mu m^2$) area with no applied electric field, which when sufficiently weak excites only NV^- fluorescence with minimal ionization. The charge distributions created by the photocurrent experiment exhibit the typical long-term stability observed in diamond[20–22,25,26,44] due to the lack of room-temperature carriers and remain unchanged up to and during the 30 s long red readout scans. Imaging thus reveals the spatial distribution of bright NV^- and dark NV^0, and therefore the flow of holes created during the photocurrent measurement. The experiment is then repeated for the next photocurrent accumulation time, and a series of images is acquired that maps out the time-dependent flow of photocurrent. Each image pixel value is normalized to the peak NV^- PL count rate, typically 5×10^4 counts s^{-1}, thus approximating the NV^-/NV^0 charge state ratio.

In Figure 1b,c, we study the time dependence of the NV population and photocurrent, respectively. We first observe the characteristic circular CCP of NV^0 that quickly grows to a radius of 10–15 μm within the first 0.5 s of the photocurrent laser application. This feature expands almost isotropically regardless of the applied field and is driven by charge carrier diffusion and space-charge effects.[44] As the photocurrent laser is held on, we observe the formation of filamentary structures of NV^0 that connect the CCP to the ground (positive) electrode. The formation of these features correlates with sudden, distinct increases in photocurrent, indicating that hole photocurrent flows from the ground electrode into the CCP via these channel-like filaments. Later, a significant "breakdown"-like event is observed, corresponding to an almost doubled photocurrent and complicated, unstable temporal dynamics. We also studied how the photocurrent and filaments depend on the position of the laser, laser power and applied electric field (see Supporting Information).

2.1. In Situ Device Characterization

The filamentary current channels are observed to nucleate from specific regions of the ground (positive) electrode, and grow from right to left, starting as dark patches near the electrode that eventually reach out to join the CCP. In some cases, a matching filament from the CCP is observed to join the approaching filament from the electrode. In Figure 1d we shift the vertical

**ADVANCED
SCIENCE NEWS**

www.advancedsciencenews.com

**ADVANCED
MATERIALS**

www.advmat.de

position where the photocurrent beam is applied across the full 200 μm field of view of our microscope and observe consistent sites where the filaments form, sometimes taking nontrivial paths [e.g., Figure 1d–ii,iv)] to join to the source CCP. The onset of filaments is always accompanied by a steep increase in photocurrent (inset).

A hint to the origin of these photocurrent filament channels is found in the observed nucleation points along the electrode, and a consistent nucleation point appears to be the top corner of the right-hand electrode, where field bunching results in a locally stronger electric field. We therefore hypothesize that filaments nucleate – current is preferentially injected – at similar points of higher electric field strength along the electrode, whether due to localized intrinsic interface defects, microscopic damage or imperfections in the metal-semiconductor junction. This latter point is of considerable interest, given the difficulty in fabricating electrical contacts on diamond and the lack of existing characterization techniques. We note that for all applied electric fields in this work, estimated to be of order 10–20 kV cm^{-1}, NV electrometry[45–47] could not detect any electric-field induced splittings or shifts. In contrast, optical measurement of the photocurrent via NV charge state conversion yields a striking and highly specific in situ detection method for local electric field inhomogeneity.

2.2. Engineering Photoconductivity with Dark Impurities

We now draw special attention to the role of charge-state preparation, not just of the NV centers but of other, non-luminescent defects in the diamond. Indeed, for the charge state of the NV centers to be a non-perturbative detector of carrier transport, the extent to which the probes affect the photocurrent dynamics must first be understood. We first remove the DP step, which generates the NV$^-$ charge state, resulting in initialization into optically dark NV^0/N^0. **Figure 2a** shows the photocurrent as a function of time following initialization with and without DP, with almost twice as much photocurrent observed without the DP step, and lacking the intervening filament nucleation step. While this might initially point to the NV charge state playing a significant role in photocurrent transport, further investigation reveals the opposite. We introduce another step, consisting of a 300 μW red (633 nm) scan (RS) that follows either GI or DP. Illumination with weak red light results in one-way ionization of the NV$^-$ to NV^0,[41] but with a photon energy of 1.96 eV, below the 2.2 eV photoionization threshold of N^0,[48] the red light leaves the nitrogen charge state unchanged.

In Figure 2a we compare the previous initialization stages with the addition of a RS step. Notably, the photocurrent is unchanged following initialization to NV$^-$ and subsequent ionization with red scanning, and essentially identical when a red scan follows a GI-only initialization. The nearly identical photocurrent profiles correlate with the expected nitrogen charge state and confirm the NV plays a negligible role in the photocurrent dynamics, serving only to detect the spatial distribution of holes.

Photocurrent appears to flow readily in N^0-rich regions, and less so in N$^+$-rich regions. Rather than scanning across the whole inter-electrode region, we can optically engineer specific regions by "painting" patterns of NV^0/N^0 with green light. In Figure 2(b),

we scan a green laser beam with power P_{ch} horizontally between the electrodes, making a conducting channel with the width set by P_{ch}: as the channel is widened with increasing power, the time taken for the photocurrent to reach the same saturation value decreases. The time-dependence mirrors the signatures of filament formation, with a characteristic step in photocurrent signal occurring at earlier times as the channel width, effectively an artificial filament, is increased. Similarly, in Figure 2c, we paint a vertical line parallel to the right-hand electrode. Now, filaments form between the source CCP and the painted region, accompanied by the same photocurrent signatures observed for filaments formed between the CCP and the bare electrode. Interestingly, this observation implies the processes that drive filament nucleation at the diamond-electrode interface are replicated in the defect charge environment following green laser application, which we assume generates N^0 in its vicinity.

2.3. 3D Imaging of Photocurrent Flow

The electrical conductivity of diamond is strongly dependent on the surface chemistry,[49] which can also be modified by light.[42] An important question then arises as to whether the surface of the diamond plays a significant role in our own experiments. Due to the lateral electrode geometry of our device, the electric field strength decreases linearly with depth (see Supporting Information), meaning the strongest carrier drift is found at or near the surface. We extended our photocurrent imaging scheme into three dimensions (**Figure 3a**) by incrementally changing the z-plane where the red readout scan is performed, with all other optical manipulation steps as before. To probe the depth dependence of photocurrent transport, we first apply a green laser beam ($P = 1.2$ mW, for 0.5 s) 15 μm below the surface of the diamond and 10 μm from the ground electrode to generate an isolated, "target" CCP, analogous to the painted regions depicted in Figure 2b,c though entirely separate from the electrodes. 3D charge-sensitive confocal scanning (Figure 3a,b) reveals the characteristic shape of the CCP, consisting of a spherical region of dark NV^0 punctured by the conical regions exposed to the entering and exiting laser beam, which remain NV$^-$.[41]

With the target CCP in place, we made a photocurrent measurement as before, with the "source" laser positioned 7.5μm below the surface for a varied time t_p. Figure 3b shows a sequence of 3D maps of the resulting NV^0 distributions following variable time photocurrent laser measurements. As time progresses, we see filament formation extending more than 10 μm into the diamond bulk prior to the onset of photocurrent breakdown. More significantly, we observe a distinct, isolated filament form to join the source and target CCP. These measurements show unambiguously that the photocurrent spatial dynamics result from charged defects inside the diamond bulk, rather than surface conduction effects. Prior to formation of a connecting filament, the target CCP bulges toward the photocurrent-induced CCP (see accompanying videos in the Extended Data). This observation, while in concordance with our measurements showing filament nucleation from both the bare electrodes and the "painted" regions in Figure 2c, is unexplained, as the "target" CCP appears to be fully disconnected from the ground electrode.

**ADVANCED
SCIENCE NEWS**

www.advancedsciencenews.com

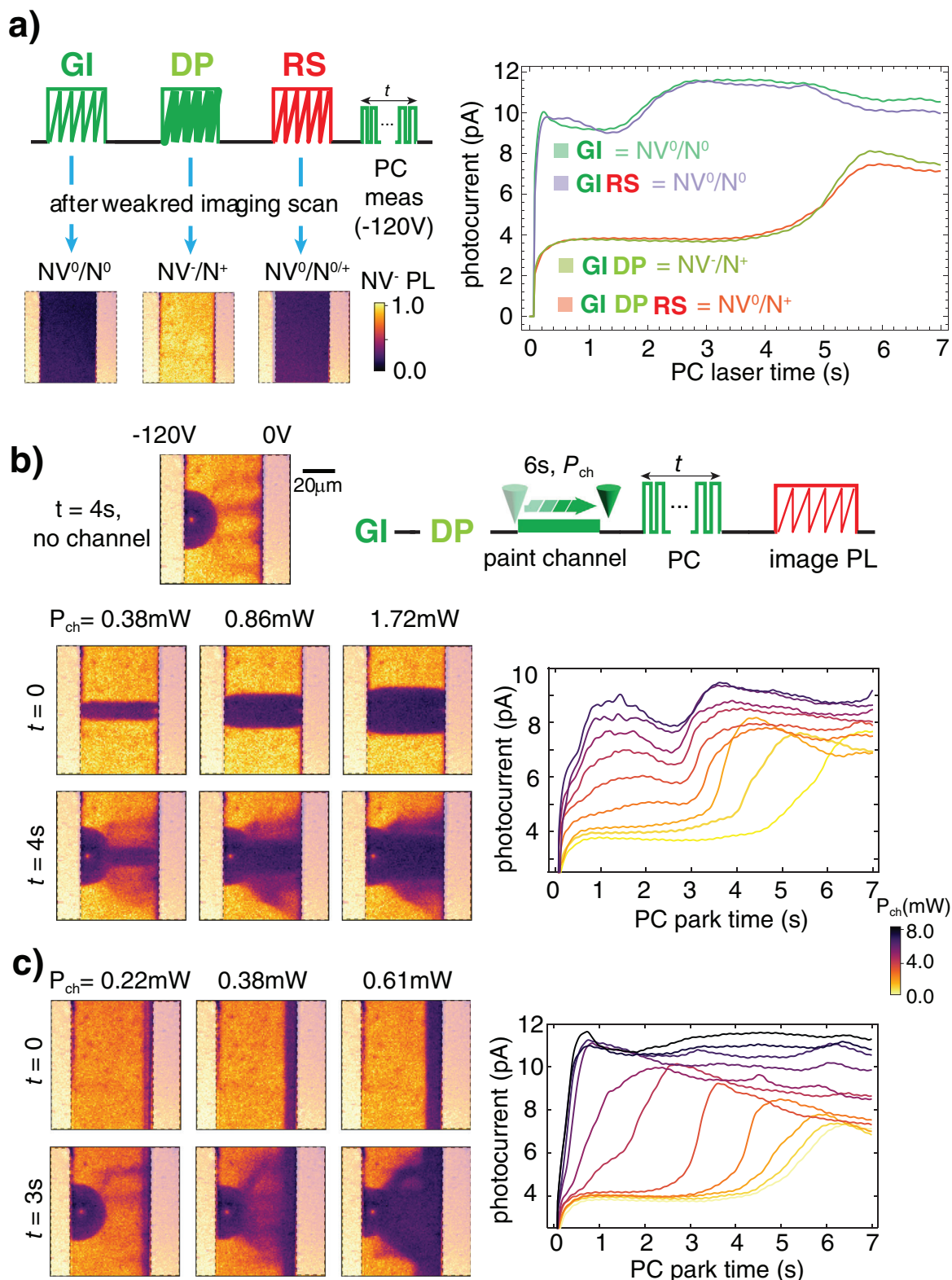**ADVANCED
MATERIALS**

www.advmat.de

Figure 2. Optically engineering the initial conductivity. a) Three optical preparation steps control the charge state of NV centers and nitrogen impurities between the electrodes. GI prepares mostly NV^0 and N^0 due to charge cycling and carrier capture, DP creates NV^- and N^+ while an RS scan ionizes NV^- and leaves N^0 and N^+ untouched. Photocurrent measurements following initialization steps are independent of the NV charge state, but strongly dependent on the assumed N charge state. b) Drawing horizontal or c) vertical paths with a varied-power green laser defines conductive channels, with wider horizontal channels resulting in greater photocurrent generation, and wider vertical channels parallel to the negative electrode nucleating filaments at earlier times, with concomitantly higher photocurrents.
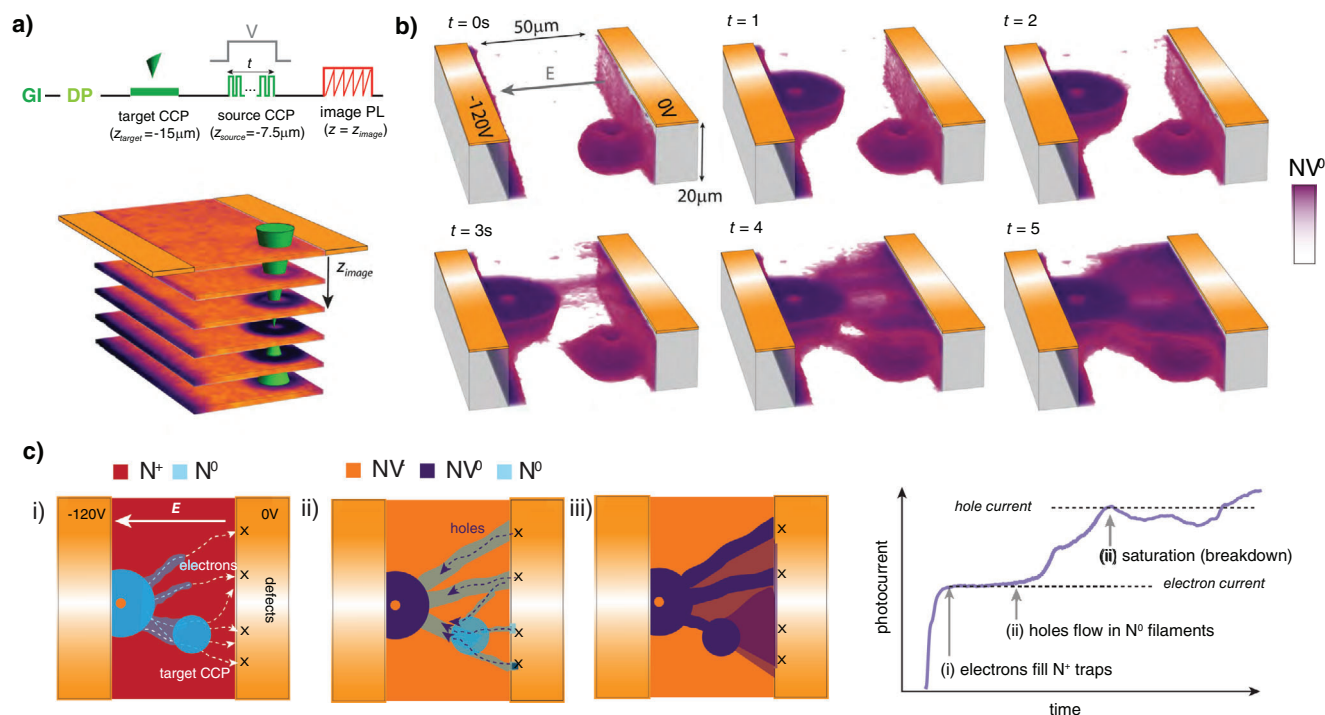
**ADVANCED
SCIENCE NEWS**

www.advancedsciencenews.com

**ADVANCED
MATERIALS**

www.advmat.de

Figure 3. 3D-spatiotemporal mapping of photocurrent flow. a) Illustration (bottom) and protocol (top) for time-resolved 3D photocurrent imaging with charge-sensitive microscopy. Here, a "target" CCP is generated with a 0.50 s, 1.2 mW laser park 15 μm below the diamond surface. Varying the z-plane where the x-y confocal scan is performed reveals the near-spherical shape of the target CCP, which is fully disconnected from the metal electrodes (the dark sections on the sides are the result of shadows cast by the electrodes). b) Applying an opacity mask to display only the NV^0 concentration, we reveal the full 3D spatiotemporal dynamics of photocurrent generation, filamentation and breakdown. The source photocurrent laser is applied for time t, 7.5 μm below the surface, the uppermost z-position corresponds to $z = 5$ μm below the diamond surface. We note the distortion and eventual filament nucleation from the target CCP, 15 μm below the surface. c) A simple cartoon model of filament formation and corresponding photocurrent accumulation. i), electrons generated by the photocurrent laser drift under the applied field, being captured by N^+ and consequently forming channels of N^0 ii) that act as conduction pathways for holes, at later times individual filaments are washed out and hole flow saturates iii). The proposed role of the target CCP in this picture is to gather and bunch hole trajectories toward the CCP, which explains the bulging observed in (b).

3. Discussion

Our measurements provide an intricate picture of the origin and phenomenology of photocurrent propagation in diamond. We first note that holes appear to cross the metal-diamond junction of the ground electrode and converge toward the CCP, first as channel-like filaments and then as a breakdown-like flow that converges toward the CCP in a broad "V"-like shape. To understand this, we must again take into consideration that the charge state of nonfluorescent defects has a significant effect on the spatio-temporal dynamics of the current flow. While holes travel from right to left in images such as Figure 1b and leave visible evidence in the form of NV^0, electrons are to be assumed to follow similar, unseen trajectories but from left to right. Electrons generated by the photocurrent laser remain invisible to our imaging technique, as the dominant interaction expected is captured by N^+, which does not change the NV fluorescence but does affect the charge transport rate. From Figure 1d, hole injection is observed to occur at specific, reproducible regions of the ground electrode, and we expect that these same sites also attract electron flow toward regions of stronger electric field. Electrons create channels of N^0 as they are drawn to these defective sites, and then build up on the diamond-electrode Schottky interface. Eventually, sufficient

negative charge buildup occurs to reduce the Schottky barrier height and facilitate hole (minority carrier) injection,[50] which in turn preferentially flows along the channels passivated by the electrons.

We can thus posit a model where charged impurity scattering sets the electron and hole mobilities and the filaments are first traced by electrons propagating away from the photocurrent laser beam, as depicted in Figure 3c. Open questions remain as to the microscopic charge environment, and whether the nitrogen is initialized into a positive charge state alone (as an optically-defined space-charge region), or compensated by electron capture by neutral defects such as neutral vacancies V^0.[51] In the latter case, the charge environment is neutral, though possesses equal numbers of ionized impurities acting as electron and hole traps, resulting in the observed impeded current flow. In both pictures, carrier capture drives the charge environment toward a state composed of neutrally-charged defects (N^0, V^0) which results in higher carrier mobilities. The time-dependence of the photocurrent, which resembles the archetypal case for extrinsic, defect-mediated photoconductivity[52] offers further insights. Given a significant photocurrent flows before any filaments are observed optically, we can deduce that the initial photocurrent is due to electrons, which gradually passivate the N^+ population that impedes hole flow. With a high hole mobility corridor of N^0

**ADVANCED
SCIENCE NEWS**

www.advancedsciencenews.com

**ADVANCED
MATERIALS**

www.advmat.de

connecting the CCP to the electrode, hole current now flows and is observed through charge state conversion of the NV centers.

We now apply our model to explain the phenomenology observed in Figures 2c and 3b. Of particular note is the somewhat anomalous finding that an isolated target CCP appears to bulge or distort in the direction of the photocurrent CCP. We note that no bulging or distortion is observed for an equivalent experiment without the applied electric field, or without the photocurrent laser but with an applied field. Due to the very short carrier lifetime ($\approx 1\,\mu s$),[53] no free charge is stored in the isolated target CCP, which is created several seconds before the photocurrent beam is turned on. We propose that the isolated target CCP acts essentially as a focal point first for electron current, which is drawn to the isolated region of NV^0/N^0 in the same way as it is focused on defective sites along the electrode and the painted regions in Figure 2c. This in turn attracts holes, which flow along various defect-nucleated paths from the electrode toward the target CCP. Here, the paths bunch up, resulting in a higher hole concentration and stronger NV^0 signal than closer to the positive electrode. Further work is needed to fully understand this observation.

4. Conclusion

Our work demonstrates a powerful new measurement modality for the study of charge transport in a semiconductor, and poses questions that motivate an improved understanding of photoelectric physics in wide-bandgap materials. In this work, we have focused on diamond, which is arguably the most technologically mature platform for our technique, possessing well-characterized photochromic defects which are stable at room-temperature, while also being the ultimate material for high-power electronics.[17–19] With further work, our method could be extended to materials more advanced in terms of power-efficient semiconductor applications which host similar optically active defect centers,[54] i.e., SiC[55] or GaN.[56] In addition to offering insights into charge transport physics, the results described in this work can also be applied to the generation and stabilization of color centers in quantum materials, such as group-IV centers in diamond[57] or boron-vacancies in hBN,[58] where charge transfer between defects can be mediated by injected carriers.[59] Focusing on diamond, our work has immediate implications for the photoelectric detection of NV centers.[60,61] Photoelectric detection of NV magnetic resonance promises fully-integrated sensors unconstrained by the diffraction limit and limitations of optical collection efficiency.[60] Indeed, the complicated spatial dynamics of photocurrent we measure here are at play, unseen, in many photoelectric detection schemes. Similar issues are encountered in diamond radiation detectors, where impurities capture charge carriers generated by high-energy particles,[62] leading to space-charge effects that impact performance. However, photocurrent cannot be spectrally filtered like photoluminescence, and the carrier capture by other defects we observe here translates to reduced photocurrent yield. Both these points are addressed in our work, where we show careful control of the nitrogen charge state yields significantly enhanced photocurrents, and observation of filament formation allows us to attribute sources of photocurrent injection to the electrodes rather than from a particular defects. Our method could also be applied to the case of mapping photocurrents generated from single defect centers[33] with single

defect centers,[22,23,41] or with further work to the much larger currents present in operating wide-bandgap semiconductor devices. More ambitiously, optical manipulation of specific defect concentrations and regions could be used to create junctions, current pathways, interconnects and potentially even entire optically-defined devices using charged defects.

5. Experimental Section

Electrode Fabrication: Square $500 \times 500\,\mu m$ electrodes were fabricated following a photolithographic patterning and lift-off process. The diamond substrate was first cleaned by boiling in a 1:20 (by weight) mixture of sodium nitrate and sulfuric acid for 20 min followed by a 10 min immersion in piranha etching solution at 90°C and subsequent ultrasonic immersion in deionized water. The sample was coated with image-reversal photoresist (AZ1514E - MicroChemicals GmbH) by spin-coating. After baking to remove resist solvent, the sample underwent a brief flood exposure under a standard mercury vapor lamp in a mask aligner (Quintel), after which the sample underwent image-reversal baking in order to partially crosslink the uppermost layer of the resist film. Electrode patterns were then written on the sample using a direct-write UV lithography system (POLOS NanoWriter), after which the resist was developed in AZ 726 MIF developer for 90 s. The crosslinked upper layer of resist results in an undercut sidewall profile, thereby allowing for evaporation and lift-off to create the electrodes. The sample was exposed to oxygen–argon plasma in a benchtop plasma ashing system (Diener Femto) for 30 s to remove photoresist residues from the sample surface prior to electron-beam evaporation of a 15 nm/100 nm Cr/Au stack. Lift-off was performed by ultrasonication in acetone followed by deionized water. No post-fabrication annealing of the electrodes was performed, and the sample preparation steps leave the diamond with an oxygen-terminated surface.

Supporting Information

Supporting Information is available from the Wiley Online Library or from the author.

Conflict of Interest

The authors declare no conflicts of interest.

Author Contributions

A.A.W. conceived and led the work with guidance from C.A.M. and A.M.M. Data was collected and analyzed by A.A.W. with assistance by R.M.G. The

**ADVANCED
SCIENCE NEWS**

www.advancedsciencenews.com

**ADVANCED
MATERIALS**

www.advmat.de

[1] I. Aharonovich, D. Englund, M. Toth, *Nat. Photon.* **2016**, *10*, 631.

[2] M. Atatüre, D. Englund, N. Vamivakas, S.-Y. Lee, J. Wrachtrup, *Nat. Rev. Mater.* **2018**, *3*, 38.

[3] D. Y. Fedyanin, *Adv. Quantum Technol.* **2021**, *4*, 2100048.

[4] A. Chatterjee, P. Stevenson, S. De Franceschi, A. Morello, N. P. de Leon, F. Kuemmeth, *Nat. Rev. Phys.* **2021**, *3*, 157.

[5] M. W. Doherty, N. B. Manson, P. Delaney, F. Jelezko, J. Wrachtrup, L. C. L. Hollenberg, *Phys. Rep.* **2013**, *528*, 1.

[6] W. F. Koehl, B. B. Buckley, F. J. Heremans, G. Calusine, D. D. Awschalom, *Nature* **2011**, *479*, 84.

[7] H. Kraus, V. A. Soltamov, D. Riedel, S. Väth, F. Fuchs, A. Sperlich, P. G. Baranov, V. Dyakonov, G. V. Astakhov, *Nat. Phys.* **2014**, *10*, 157.

[8] T. Iwasaki, W. Naruki, K. Tahara, T. Makino, H. Kato, M. Ogura, D. Takeuchi, S. Yamasaki, M. Hatano, *ACS Nano* **2017**, *11*, 1238.

[9] D. A. Broadway, N. Dontschuk, A. Tsai, S. E. Lillie, C. T.-K. Lew, J. C. McCallum, B. C. Johnson, M. W. Doherty, A. Stacey, L. C. L. Hollenberg, J.-P. Tetienne, *Nat. Electron.* **2018**, *1*, 502.

[10] J. Forneris, S. Ditalia Tchernij, P. Traina, E. Moreva, N. Skukan, M. Jakšić, V. Grilj, F. Bosia, E. Enrico, G. Amato, I. Degiovanni, B. Naydenov, F. Jelezko, M. Genovese, P. Olivero, *Phys. Rev. Appl.* **2018**, *10*, 014024.

[11] C. P. Anderson, A. Bourassa, K. C. Miao, G. Wolfowicz, P. J. Mintun, A. L. Crook, H. Abe, J. Ul Hassan, N. T. Son, T. Ohshima, D. D. Awschalom, *Science* **2019**, *366*, 1225.

[12] S. E. Lillie, N. Dontschuk, D. A. Broadway, D. L. Creedon, L. C. Hollenberg, J.-P. Tetienne, *Phys. Rev. Appl.* **2019**, *12*, 024018.

[13] B. B. Zhou, P. C. Jerger, K.-H. Lee, M. Fukami, J. Park, D. D. Awschalom, *Phys. Rev. X* **2020**, *10*, 011003.

[14] Q. Zhang, G. Hu, G. G. de Boo, M. Ranšić, B. C. Johnson, J. C. McCallum, J. Du, M. J. Sellars, C. Yin, S. Rogge, *Nano Lett.* **2019**, *19*, 5025.

[15] S. Scholten, G. Abrahams, B. Johnson, A. Healey, I. Robertson, D. Simpson, A. Stacey, S. Onoda, T. Ohshima, T. Kho, J. Ibarra Michel, J. Bullock, L. Hollenberg, J.-P. Tetienne, *Phys. Rev. Appl.* **2022**, *18*, 014041.

[16] A. Jenkins, S. Baumann, H. Zhou, S. A. Meynell, Y. Daipeng, K. Watanabe, T. Taniguchi, A. Lucas, A. F. Young, A. C. Bleszynski Jayich, *Phys. Rev. Lett.* **2022**, *129*, 087701.

[17] C. J. H. Wort, R. S. Balmer, *Mater. Today* **2008**, *11*, 22.

[18] N. Donato, N. Rouger, J. Pernot, G. Longobardi, F. Udrea, *J. Phys. D: Appl. Phys.* **2019**, *53*, 093001.

[19] D. Araujo, M. Suzuki, F. Lloret, G. Alba, P. Villar, *Materials* **2021**, *14*, 7081.

[20] H. Jayakumar, J. Henshaw, S. Dhomkar, D. Pagliero, A. Laraoui, N. B. Manson, R. Albu, M. W. Doherty, C. A. Meriles, *Nat. Commun.* **2016**, *7*, 12660.

[21] S. Dhomkar, J. Henshaw, H. Jayakumar, C. A. Meriles, *Sci. Adv.* **2016**, *2*, 1600911.

[22] A. Lozovoi, H. Jayakumar, D. Daw, G. Vizkelethy, E. Bielejec, M. W. Doherty, J. Flick, C. A. Meriles, *Nat. Electron.* **2021**, *4*, 717.

[23] A. Lozovoi, Y. Chen, G. Vizkelethy, E. Bielejec, J. Flick, M. W. Doherty, C. A. Meriles, *Nano Lett.* **2023**, *23*, 4495.

[24] G. Wolfowicz, F. J. Heremans, C. P. Anderson, S. Kanai, H. Seo, A. Gali, G. Galli, D. D. Awschalom, *Nat. Rev. Mater.* **2021**, *6*, 906.

[25] A. Wood, A. Lozovoi, Z.-H. Zhang, S. Sharma, G. I. López-Morales, H. Jayakumar, N. P. de Leon, C. A. Meriles, *Nano Lett.* **2023**, *23*, 1017.

[26] Z.-H. Zhang, A. M. Edmonds, N. Palmer, M. L. Markham, N. P. de Leon, *Phys. Rev. Appl.* **2023**, *19*, 034022.

[27] D. Bluvstein, Z. Zhang, A. C. B. Jayich, *Phys. Rev. Lett.* **2019**, *122*, 076101.

[28] J. A. Zuber, M. Li, M. l. G. Puigibert, J. Happacher, P. Reiser, B. J. Shields, P. Maletinsky, *Nano Lett.* **2023**, *23*, 10901.

[29] W. Ji, Z. Liu, Y. Guo, Z. Hu, J. Zhou, S. Dai, Y. Chen, P. Yu, M. Wang, K. Xia, F. Shi, Y. Wang, J. Du, *Nat. Photon.* **2024**, *18*, 230.

[30] T. Delord, R. Monge, C. A. Meriles, *Nano Lett.* **2024**, *24*, 6474.

[31] Q. Ma, R. Krishna Kumar, S.-Y. Xu, F. H. L. Koppens, J. C. W. Song, *Nat. Rev. Phys.* **2023**, *5*, 170.

[32] M. N. R. Ashfold, J. P. Goss, B. L. Green, P. W. May, M. E. Newton, C. V. Peaker, *Chem. Rev.* **2020**, *120*, 5745.

[33] P. Siyushev, M. Nesladek, E. Bourgeois, M. Gulka, J. Hruby, T. Yamamoto, M. Trupke, T. Teraji, J. Isoya, F. Jelezko, *Science* **2019**, *363*, 728.

[34] E. Bourgeois, M. Gulka, M. Nesladek, *Adv. Optical Mater.* **2020**, *8*, 12.

[35] A. Grillo, A. Di Bartolomeo, *Adv. Electron. Mater.* **2021**, *7*, 2000979.

[36] N. Aslam, G. Waldherr, P. Neumann, F. Jelezko, J. Wrachtrup, *New J. Phys.* **2013**, *15*, 013064.

[37] E. Bourgeois, A. Jarmola, P. Siyushev, M. Gulka, J. Hruby, F. Jelezko, D. Budker, M. Nesladek, *Nat. Commun.* **2015**, *6*, 8577.

[38] S. Dhomkar, P. R. Zangara, J. Henshaw, C. A. Meriles, *Phys. Rev. Lett.* **2018**, *120*, 117401.

[39] A. Lozovoi, D. Daw, H. Jayakumar, C. A. Meriles, *Phys. Rev. Mater.* **2020**, *4*, 053602.

[40] G. Wang, C. Li, H. Tang, B. Li, F. Madonini, F. F. Alsallom, W. K. Calvin Sun, P. Peng, F. Villa, J. Li, P. Cappellaro, *PNAS* **2023**, *120*, 2305621120.

[41] A. A. Wood, A. Lozovoi, R. M. Goldblatt, C. A. Meriles, A. M. Martin, *Phys. Rev. B* **2024**, *109*, 134106.

[42] W. Zheng, K. Bian, X. Chen, Y. Shen, S. Zhang, R. Stöhr, A. Denisenko, J. Wrachtrup, S. Yang, Y. Jiang, *Nat. Phys.* **2022**, *18*, 1317.

[43] J. Hruby, M. Gulka, M. Mongillo, I. P. Radu, M. V. Petrov, E. Bourgeois, M. Nesladek, *Appl. Phys. Lett.* **2022**, *120*, 162402.

[44] A. Lozovoi, H. Jayakumar, D. Daw, A. Lakra, C. A. Meriles, *Phys. Rev. Lett.* **2020**, *125*, 256602.

[45] F. Dolde, H. Fedder, M. W. Doherty, T. Nöbauer, F. Rempp, G. Balasubramanian, T. Wolf, F. Reinhard, L. C. L. Hollenberg, F. Jelezko, J. Wrachtrup, *Nat Phys* **2011**, *7*, 459.

[46] J. Michl, J. Steiner, A. Denisenko, A. Bülau, A. Zimmermann, K. Nakamura, H. Sumiya, S. Onoda, P. Neumann, J. Isoya, J. Wrachtrup, *Nano Lett.* **2019**, *19*, 4904.

[47] T. Mittiga, S. Hsieh, C. Zu, B. Kobrin, F. Machado, P. Bhattacharyya, N. Rui, A. Jarmola, S. Choi, D. Budker, N. Yao, *Phys. Rev. Lett.* **2018**, *121*, 246402.

[48] E. Bourgeois, E. Londero, K. Buczak, J. Hruby, M. Gulka, Y. Balasubramaniam, G. Wachter, J. Stursa, K. Dobes, F. Aumayr, M. Trupke, A. Gali, M. Nesladek, *Phys. Rev. B* **2017**, *95*, 041402.

[49] C. I. Pakes, J. A. Garrido, H. Kawarada, *MRS Bull.* **2014**, *39*, 542.

[50] M. A. Green, J. Shewchun, *Solid-State Electron.* **1973**, *16*, 1141.

[51] G. Davies, A. T. Collins, *Diam. Rel. Mater.* **1993**, *2*, 80.

[52] K. W. Boer, U. W. Pohl, *Semiconductor Physics*, Springer, Berlin **2018**.

[53] P. Grivickas, P. Ščajev, N. Kazuchits, S. Lastovskii, L. F. Voss, A. M. Conway, A. Mazanik, O. Korolik, V. Bikbajevas, V. Grivickas, *Appl. Phys. Lett.* **2020**, *117*, 242103.

[54] G. Zhang, Y. Cheng, J.-P. Chou, A. Gali, *Appl. Phys. Rev.* **2020**, *7*, 031308.

[55] M. Niethammer, M. Widmann, T. Rendler, N. Morioka, Y.-C. Chen, R. Stöhr, J. U. Hassan, S. Onoda, T. Ohshima, S.-Y. Lee, A. Mukherjee, J. Isoya, N. T. Son, J. Wrachtrup, *Nat Commun* **2019**, *10*, 5569.

[56] Y. Zhou, Z. Wang, A. Rasmita, S. Kim, A. Berhane, Z. Bodrog, G. Adamo, A. Gali, I. Aharonovich, W.-b. Gao, *Sci. Adv.* **2018**, *4*, eaar3580.

[57] M. Rieger, V. Villafañe, L. M. Todenhagen, S. Matthies, S. Appel, M. S. Brandt, K. Müller, J. J. Finley, *Sci. Adv.* **2024**, *10*, eadl4265.

[58] T. T. Tran, K. Bray, M. J. Ford, M. Toth, I. Aharonovich, *Nat. Nanotechnol.* **2016**, *11*, 37.

[59] A. Gale, D. Scognamiglio, I. Zhigulin, B. Whitefield, M. Kianinia, I. Aharonovich, M. Toth, *Nano Lett.* **2023**, *23*, 6141.

[60] H. Zheng, J. Hruby, E. Bourgeois, J. Soucek, P. Siyushev, F. Jelezko, A. Wickenbrock, M. Nesladek, D. Budker, *Phys. Rev. Appl.* **2022**, *18*, 024079.

[61] H. Morishita, N. Morioka, T. Nishikawa, H. Yao, S. Onoda, H. Abe, T. Ohshima, N. Mizuochi, *Phys. Rev. Appl.* **2023**, *19*, 034061.

[62] T. Shimaoka, S. Koizumi, J. H. Kaneko, *Functional Diamond* **2022**, *1*, 205.